Mechanical behavior and failure mechanism of resistance spot welded DP1000 dual phase steel

Chabok, A.; Van der Aa, Ellen; de Hosson, J.T.M.; Pei, Y.T.

Published in:
Materials & design

DOI:
10.1016/j.matdes.2017.03.070

Publication date:
2017

Mechanical behavior and failure mechanism of resistance spot welded DP1000 dual phase steel

A. Chabok[1], E. van der Aa[2], J.T.M. De Hosson[3], Y.T. Pei[1*]

[1] Department of Advanced Production Engineering, Engineering and Technology Institute Groningen, University of Groningen, Nijenborgh 4, 9747 AG Groningen, the Netherlands

[2] Tata Steel, P.O. Box 1000, 1970 CA IJmuiden, the Netherlands

[3] Department of Applied Physics, Zernike Institute for Advanced Materials, University of Groningen, Nijenborgh 4, 9747 AG Groningen, the Netherlands

Abstract:

This paper reports on the microstructural evolution of resistance spot welded 1000MPa dual phase steel under two different welding conditions, and their relation to the mechanical performance and failure mechanisms. It is shown that a double pulse weld scheme leads to an enhancement in cross-tension strength compared to single pulse welding. The second pulse subdivides the initial fusion zone of the first pulse into two zones. The inner part is solidified with a columnar structure after the second pulse, whereas with the second pulse the outer layer becomes recrystallized (named as Rex-zone) leading to the formation of an equiaxed structure of prior austenite grains. Characteristics of martensite formed in the Rex-zone and coarse-grained heat affected zone, where the crack initiated and propagated, were investigated using orientation imaging microscopy. It was found that a change in welding scheme from single to double pulse effectively alters the characteristics of martensitic microstructure of weld zones. The results obtained demonstrate that the Rex-zone has a lower fraction of high-angle grain boundaries and coarser structure of Bain groups as opposed to the coarse-grained heat affected zone with large fraction of high-angle grain boundaries and finer Bain groups. Besides, double pulse welding creates softer sub-critical heat affected zone which reduces stress concentration at the nugget edge during cross-tension test. The better mechanical performance of double pulse weld is attributed to the significant softening at sub-critical heat affected zone, formation of thick Rex-zone with lower residual strain and high fraction of high-angle grain boundaries and finer Bain groups in the coarse grained heat affected zone.

[*] Corresponding author. Email: y.pei@rug.nl

Keywords

Dual phase steel; resistance spot welding; cross-tension test; orientation imaging microscopy; martensite.

1. Introduction

Resistance spot welding (RSW) belongs to one of the oldest electrical joining methods of metal sheets, and it is still the most predominant technique used in automotive industry. Commercialization of RSW arises from its low-cost, robustness and high speed that make it widely used in joining and assembly lines for mass production. In recent years, the automotive industry has pursued further reduction of car body weight in order to enhance fuel economy with no compromise of safety. The focus has been on the use of advanced high strength steels (AHSS). This group of steels shows a good combination of strength and formability making them ideal replacement for conventional high strength steels. Dual phase (DP) steels with the microstructure consisting of martensite and ferrite belong to the group of AHSSs and are commonly used for safety parts in car bodies, e.g. bumpers, and side impact beams etc. [1]. Although their initial microstructure makes them ideal for automotive applications, the microstructural evolutions during rapid heating and cooling cycle of RSW adversely affect their mechanical performance. Mechanical properties and microstructure of resistance spot welded DP steels have been investigated extensively [2-8]. It has been reported that for AHSS of strength > 800MPa, the cross-tension strength of the RSW joints tends to decrease with increasing tensile strength of the base material [9]. This is attributed to the relatively high level of alloying elements in combination with an increased stress concentration at the weld nugget circumference during loading. Because of ultrafast cooling of the weld during RSW, fully martensitic microstructure can be easily formed which could

lead to brittleness of the joints. Due to lower fracture toughness of nugget, crack can easily propagate through the weld causing brittle fracture during cross-tension test [10-12]. One approach to address this issue is to temper the martensitic microstructure of the weld by post heat treatment to enhance the ductility [13, 14]. However, low current tempering generally requires long pulse times and the resulting longer cycle times make this type of post weld treatment less feasible in industrial applications. Sawanishi et al. [12] applied a short post pulsed current and studied its effect on the mechanical performance of the weld via peel tests. They showed that the propagation of the crack was arrested much longer when the weld with pulsed current was applied. They attributed the enhancement of the mechanical performance to higher fracture toughness of the weld resulting from lower segregation of alloying elements such as P and S. A similar approach was used by applying combination of finite element and phase modeling [15]. It was shown that the segregation of P at grain boundaries of solidifying zone could be significantly reduced using a simple double pulse welding process. Although the reduction of segregation by short time post pulsing has been widely studied, none of the above studies reported the effects on the martensitic properties of different welding zones.

To the best of our knowledge, no detailed work has been carried out on the crystallographic characteristics of the martensitic phase which forms during RSW. The present work aims at studying the effect of welding scheme (single and double pulsed) on the microstructural evolution and mechanical properties of DP1000 steel welds. The effects on the mechanical properties were studied using cross-tension tests and (nano)indentation tests. Furthermore, orientation imaging microscopy (OIM) was used to investigate the crystallographic features of the formed martensite and their effect on the mechanical performance of the welds.

2. Experimental

The chemical composition of the investigated DP steel is listed in the Table 1. The nominal sheet thickness and the zinc coating thickness are 1.5 mm and 50 g/mm^2, respectively. Resistance spot welds were produced using a 1000 Hz MFDC pedestal welding machine with constant current regulation and constant load of 4.5 kN. Weld electrodes (F1 16-20-5.5) and single pulse weld schedule were taken from the VDEh SEP1220-2 welding standard [16]. In order to study the effect of welding scheme on the mechanical and microstructural characteristics of the welds, two welding schedules, a single and double pulse weld schemes, were applied. Fig. 1 shows a schematic of the welding schedules for single and double pulse processes. The highest possible current of 8 kA was selected to produce the largest weld size. This current is safely below the maximum current at which expulsion occurs. For the single pulse welding, 550 ms of squeeze time followed by 380 ms as welding time and 300 ms of holding time was applied. For the alternative double pulse welding a non-standard procedure was selected. During this welding process, after 40 ms of cooling time, the second pulse was applied with the same duration and current as of the first pulse.

Table1. Chemical composition (wt.%) of DP 1000 steel used in the present study.

C	Mn	Si	Al	Nb	Ti	Cr	Ni	P	S
0.157	2.224	0.106	0.036	0.016	0.014	0.557	0.02	0.01	0.001

Cross sections of the welds were prepared with conventional metallographic methods and their microstructure was studied via optical microscopy (OM) and scanning electron microscopy (SEM). For OIM analyses, the samples were mechanically polished and then electropolished using a solution of 90% CH_3COOH + 10% $HClO_4$ at 20 V voltage and 21 °C for a period of 25 s. The OIM characterization was carried out by electron back scatter

diffraction pattern using a Philips ESEM-XL30 scanning electron microscope equipped with a field emission gun operating at 20 kV.

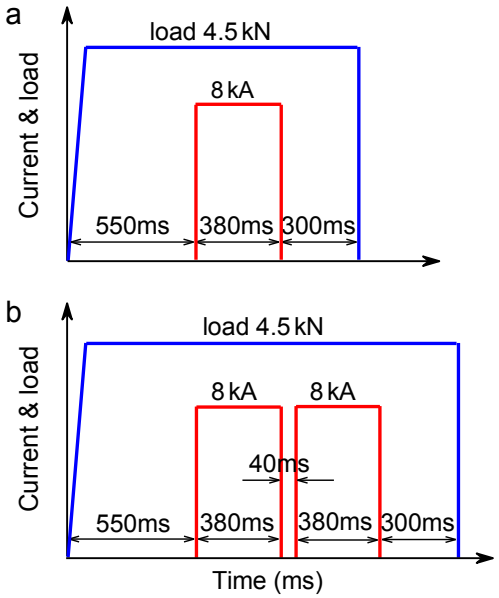

Fig. 1. RSW scheme for single pulse weld (a) and double pulse weld (b).

Vickers microhardness measurements were performed at 200 g load for a loading time of 15 s. Nanoindentation test was performed with a Berkovich indenter at the constant maximum load of 3000 µN. A minimum number of 50 indentations were conducted for each sample. In order to evaluate the mechanical performance of the welds produced by different welding scheme, cross-tension tests were performed for both single and double pulse welds (150×50 mm samples). The properties were evaluated through averaging the value of four specimens under the same welding condition.

3. Results

The cross-sectional overview of the weld nuggets is shown in Fig. 2. Single pulse weld shows a typical fusion zone (FZ) microstructure with columnar grains resulting from the rapid solidification process of the RSW (Fig. 2a). In the case of double pulse weld, the initial FZ structure of the first pulse is subdivided into two zones: the inner part composed of columnar

grains, and the outer layer that has an equiaxed microstructure. The dashed lines in Fig. 2b indicate the boundaries of the inner part and outer layer. The inner part (named as FZ2) is solidified in a typical solidification structure after the second pulse, while with applying the second pulse the outer layer is recrystallized (named as Rex-zone) . The microstructure of the Rex-zone is shown in Fig. 2c composing of martensitic microstructure formed within the equiaxed prior austenite grains (PAGs). Some prior austenite grain boundaries (PAGBs) are indicated with white arrows confirming the migration and rotation of austenite grain boundaries in the Rex-zone because of occurrence of recrystallization during the second pulse.

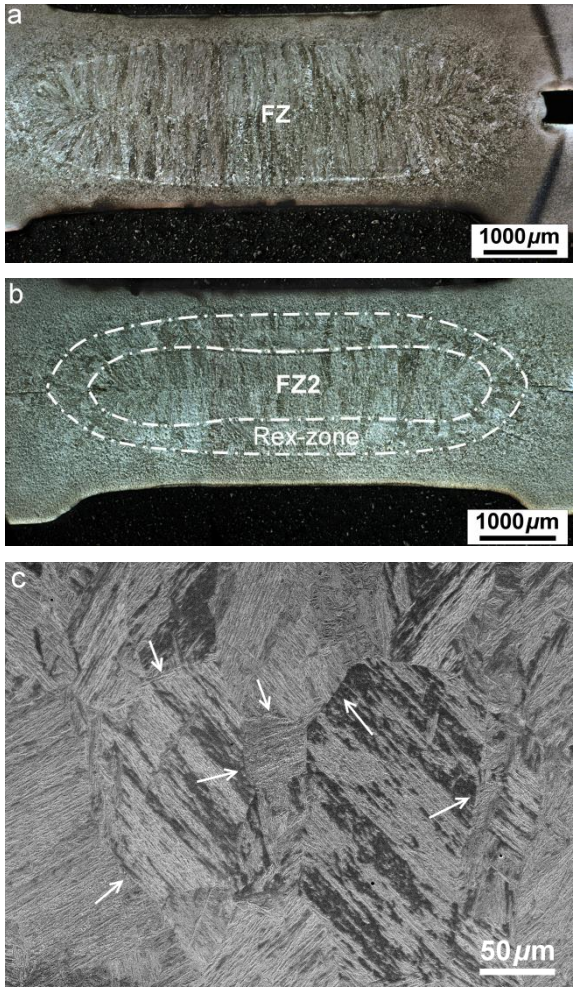

Fig. 2. OM micrograph showing the cross section of single pulse weld (a) and double pulse weld (b). (c) SEM image showing the Rex-zone of double pulse weld with arrows indicating the prior austenite grain boundaries.

3.1 Mechanical properties

Fig. 3a depicts representative load-displacement curves of single and double pulse welds. Average maximum load and absorbed energy till the maximum load for two weld schedules are shown in Fig. 3b. Energy absorption till the maximum load measures the capability of the welds to absorb the energy of impact load during a mechanical incident such as crash accident [17]. As can be seen, double pulse welds exhibit better mechanical performance as the average maximum load increases from 9.2 kN for single pulse welds to 11.7 kN for double pulse welds. Moreover, the average energy absorption rises from 55.3 J for single pulse welds to 75.2 J for double pulse welds. These results confirm that applying the second pulse can significantly enhance the mechanical performance of resistance spot welded DP1000 steels.

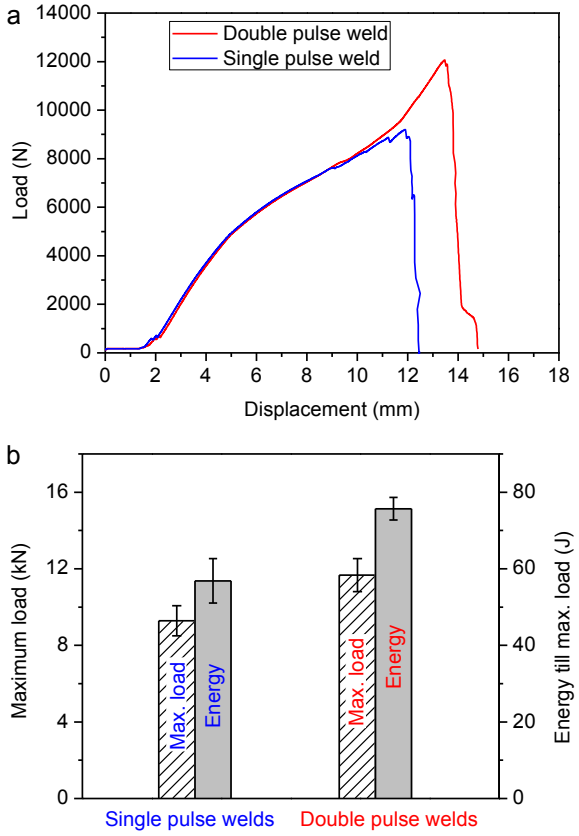

Fig. 3. (a) Representative load-displacement curve, (b) average maximum load and absorbed energy of single and double pulse welds in cross-tension test (number of samples per test = 4).

The nugget size of both welds is ~7 mm, ruling out possible effect of the weld size on the mechanical behavior of the welds. Cross sections of fractured samples after cross-tension test are shown in Fig. 4, together with an insert indicating the fracture path of the welds. Both welds fail in pull-out failure mode, as the FZ remains intact after the cross-tension test (Fig. 4a and 4b). In the case of the single pulse welds, failure occurs at the coarse grain heat affect zone (CG-HAZ) adjacent to the FZ. On the contrary, two failure zones are associated with the double pulse welds. On the left side, failure occurs close to the weld nugget as the crack penetrates a small distance in the Rex-zone and then is redirected towards the sheet thickness. On the right side, fracture originates at sub-critical heat affected zone (SC-HAZ), outside the weld nugget and close to the base metal leading to creating a lip. Both failures can occur either simultaneously or separately. The average plug diameter (fracture area) for the single pulse and double pulse weld was measured as 6.5 and 7.1 mm, respectively. Obviously, double pulse welding leads to larger fracture area, although both welds fail in pull-out failure mode.

Fig. 5 depicts the measured Vickers hardness distribution across the different microstructural zones of the welds. The average hardness of the FZ in the single pulse weld is 415 HV. A slightly lower hardness of 407 HV is measured in the FZ2 of the double pulse weld, while a significant drop in the hardness of the Rex-zone to 380 HV is observed. Furthermore, both welds show softening in the SC-HAZ with respect to the base metal with the hardness value of 303 HV. As it is shown in Fig. 5, the degree of softening is more pronounced for the double pulse weld, with a minimum hardness level 260 HV versus 281 HV in the SC-HAZ of the single pulse weld.

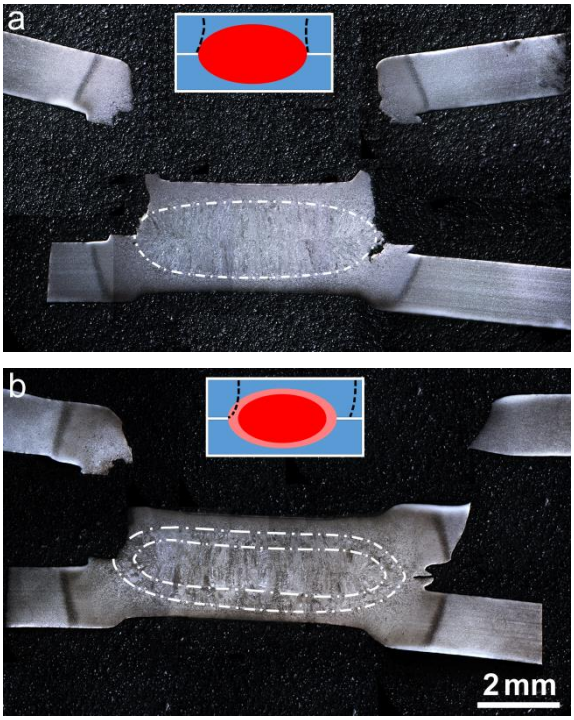

Fig. 4. Cross sectional view of cross-tension tested single pulse weld (a) and double pulse weld (b) with an insert schemetically showing the fracture path.

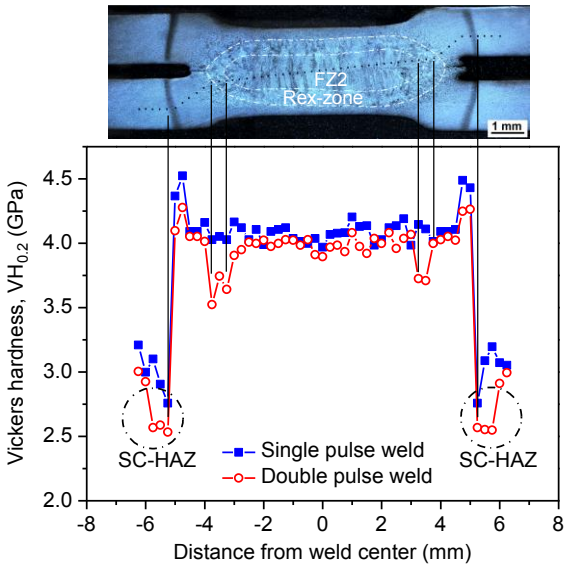

Fig. 5. Microhardness profile of the single and double pulse welds, with indents shown on a cross-section of double pulse weld.

3.2 Microstructure of the sub-critical heat affected zone

Softening of HAZ in DP steels plays an important role in affecting the failure mode and mechanical properties of DP steels, since it reduces the stress concentration at the weld nugget edge during mode I loading [18]. Reduction in the hardness of SC-HAZ with respect to the base metal has been already reported [3, 7, 19-23]. It was proved that the tempering of martensite phase in SC-HAZ is responsible for the softening phenomenon. Baltazar et al. [7, 19, 21] assessed the SC-HAZ of resistance spot welded DP steel via nanoindentation and showed that ferrite phase has negligible contribution to the softening of SC-HAZ, whereas the tempered martensite plays the major role.

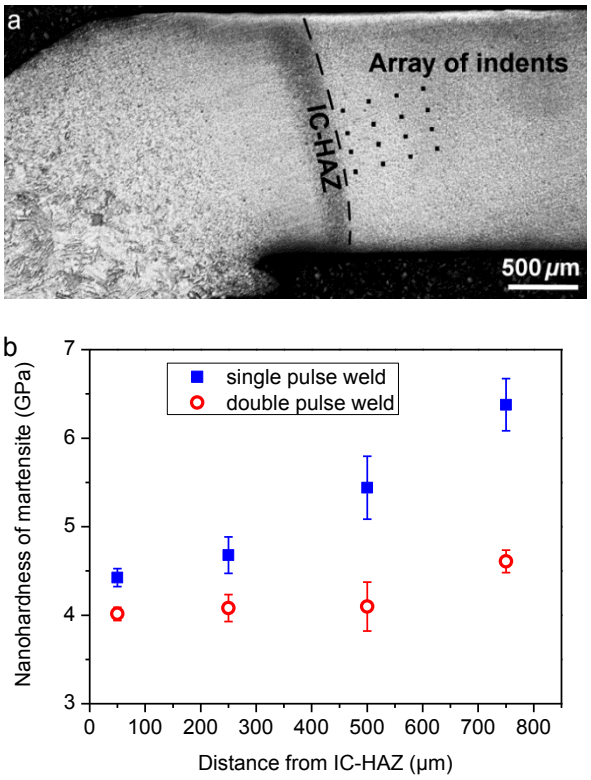

Fig. 6. (a) Cross-sectional micrograph of resistance spot weld schematically showing nanoindentation array adjacent to IC-HAZ; (b) nanohardness value of martensite at different distances from IC-HAZ towards base metal.

Fig. 6 shows the average nanohardness of the martensite phase at different distances from the inter-critical heat affected zone (IC-HAZ) towards the base metal. The SC-HAZ of the double pulse weld exhibits much softer tempered martensite. The average nanohardness of the

martensite phase located at the distance of 50 µm is yet lower than that of the martensite formed in the same location in the single pulsed RSW. Furthermore, the average nanohardness of martensite phase in the SC-HAZ of the double pulse weld shows insignificant changes over a large distance from IC-HAZ. The nanohardness at the distance of 750 µm increases to 4.6 GPa which is much lower than the corresponding nanohardness 6.4 GPa of martensite in the single pulse weld.

Fig. 7 depicts the microstructures of SC-HAZ and base metal of the two welds. The microstructure of base metal consists of martensite islands (α') dispersed in the matrix of ferrite phase (α) (Fig. 7a). Fig. 7b and 7c show the microstructure of the SC-HAZ of single pulse and double pulse welds at the distance of 50 µm from IC-HAZ, respectively. Clearly, both processes lead to features of tempered martensite with broken and decomposed islands and to the presence of sub-micron particles. In both welds fine dispersion of sub-micron white particles along the PAGBs, martensite block boundaries and interlath boundaries is visible (white arrows). These particles are formed as a result of nucleation and growth of carbides during tempering process. Microstructures of single and double pulse welds at the distance of 1000 µm from IC-HAZ are revealed in Fig. 7d and 7e, respectively. It can be inferred that the double pulse weld has still characteristics of tempered martensite, although the decomposition of martensite seems to be limited. In contrast, single pulse weld at this distance shows similar characteristics to the microstructure of base metal. Therefore, it can be concluded that double pulse welding not only softens the martensite close to the IC-HAZ, but also widens the zone subjected to the tempering process.

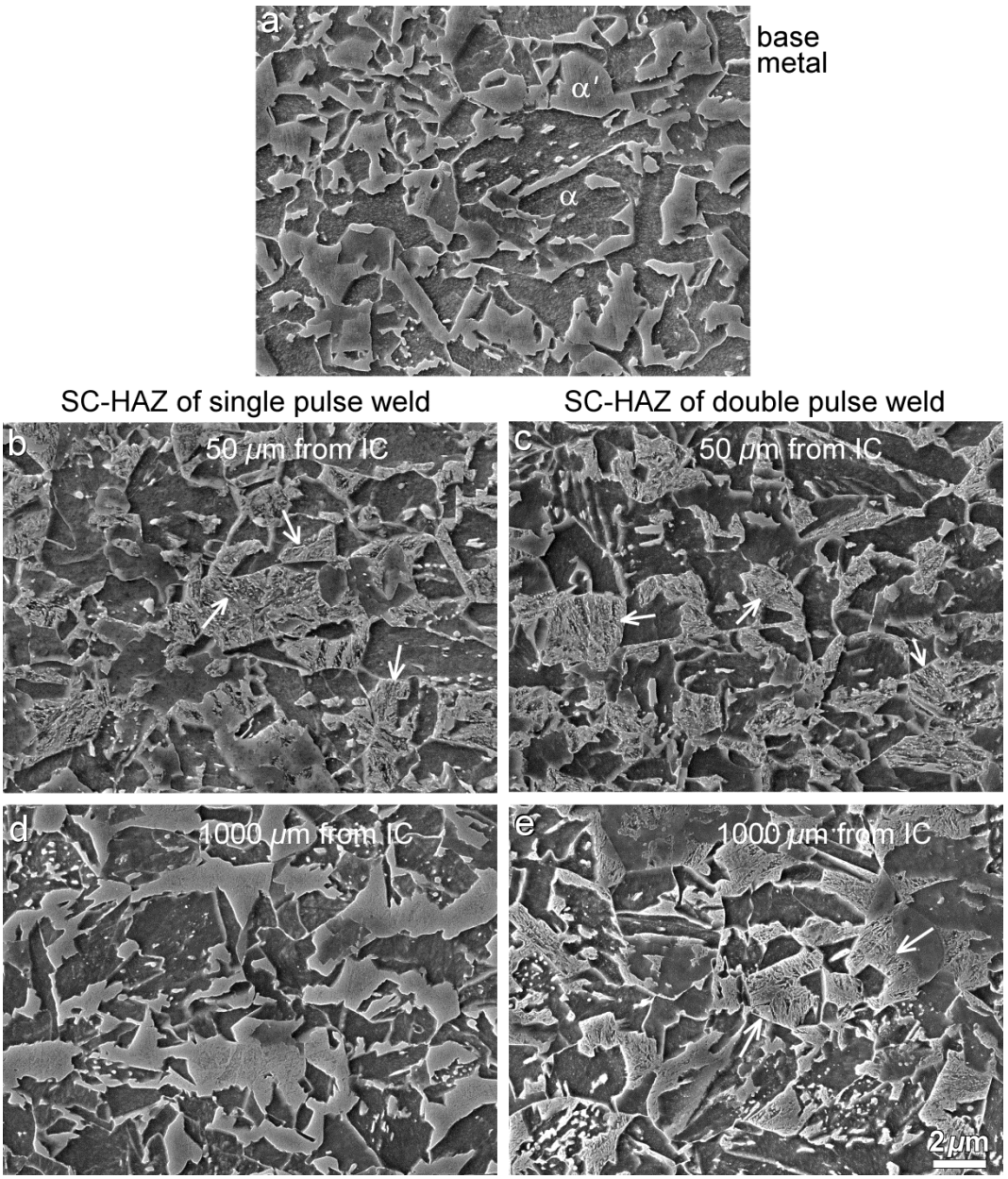

Fig. 7. SEM micrographs showing the microstructure of base metal (a), and of SC-HAZ of single pulse weld (b, d) and double pulse weld (c, e) at the distance of 50 μm and 1000 μm from IC-HAZ, respectively. Arrows indicate fine carbide particles along the PAGBs, block boundaries and interlath boundaries.

3.3 OIM analyses of the coarse-grained heat affected zone and Rex-zone

OIM was used to study the effect of the welding parameters on the microstructural evolution of martensite which is formed at CG-HAZ and Rex-zone. The fracture toughness of the weld is strongly affected by the parameters which determine the mechanical properties of

martensite formed in these zones. Crucial parts of the welds, where the crack initiates and propagates, were investigated with OIM. According to the fracture paths shown in Fig. 4, OIM maps were collected from the CG-HAZ of single pulse weld and Rex-zone and CG-HAZ of double pulse weld. The locations of OIM maps are schematically shown with black squares in Fig. 8.

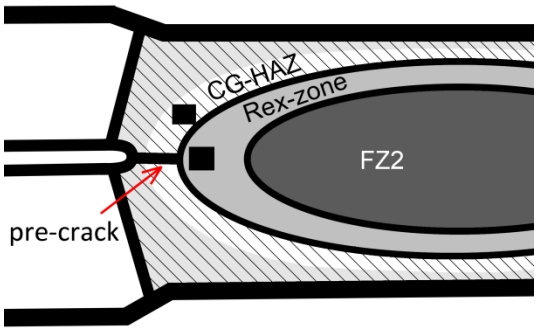

Fig. 8. Schematic image of locations where OIM maps were collected.

3.3.1 Kernel average misorientation

Fig. 9a and 9b show the inverse pole figures (IPFs) of the single pulse and double pulse welds, respectively. PAGBs are indicated by black lines. A software package ARPGE [24] was used to reconstruct PAGBs. Fig. 9c and 9d depict the corresponding kernel average misorientation (KAM) maps of the two welds. KAM shows the average misorientation of a measurement point with its six neighbors and is a qualitative measurement of local strain distribution. Maximum misorientation of 5° was imposed to calculate the KAM maps in the second neighbor configuration. Misorientations larger than 5° were not taken into account since they are considered to develop low- and high-angle grain boundaries. The KAM is presented in the color-coded map with five colors corresponding to the misorientation angle between 0° and 5° (see Fig. 9c and 9d). The local residual strain could be safely explained by KAM map as an increase in the strain leads to an increase in the local lattice rotation. Thus, higher local misorientation of a given pixel with respect to its neighbors shows higher local residual strain in the lattice. As illustrated in Fig. 9c, the KAM value for single pulse weld

decreases with moving over CG-HAZ towards FZ, and then increases again in the FZ. For double pulse weld, the lowest KAM values are achieved in the Rex-zone (Fig. 9d). Thus the FZ2 with higher residual strain is surrounded by a recrystallized shell that has lower residual strain. For both samples, the outer CG-HAZ far from the nugget shows the highest KAM value that indicates the highest residual strain.

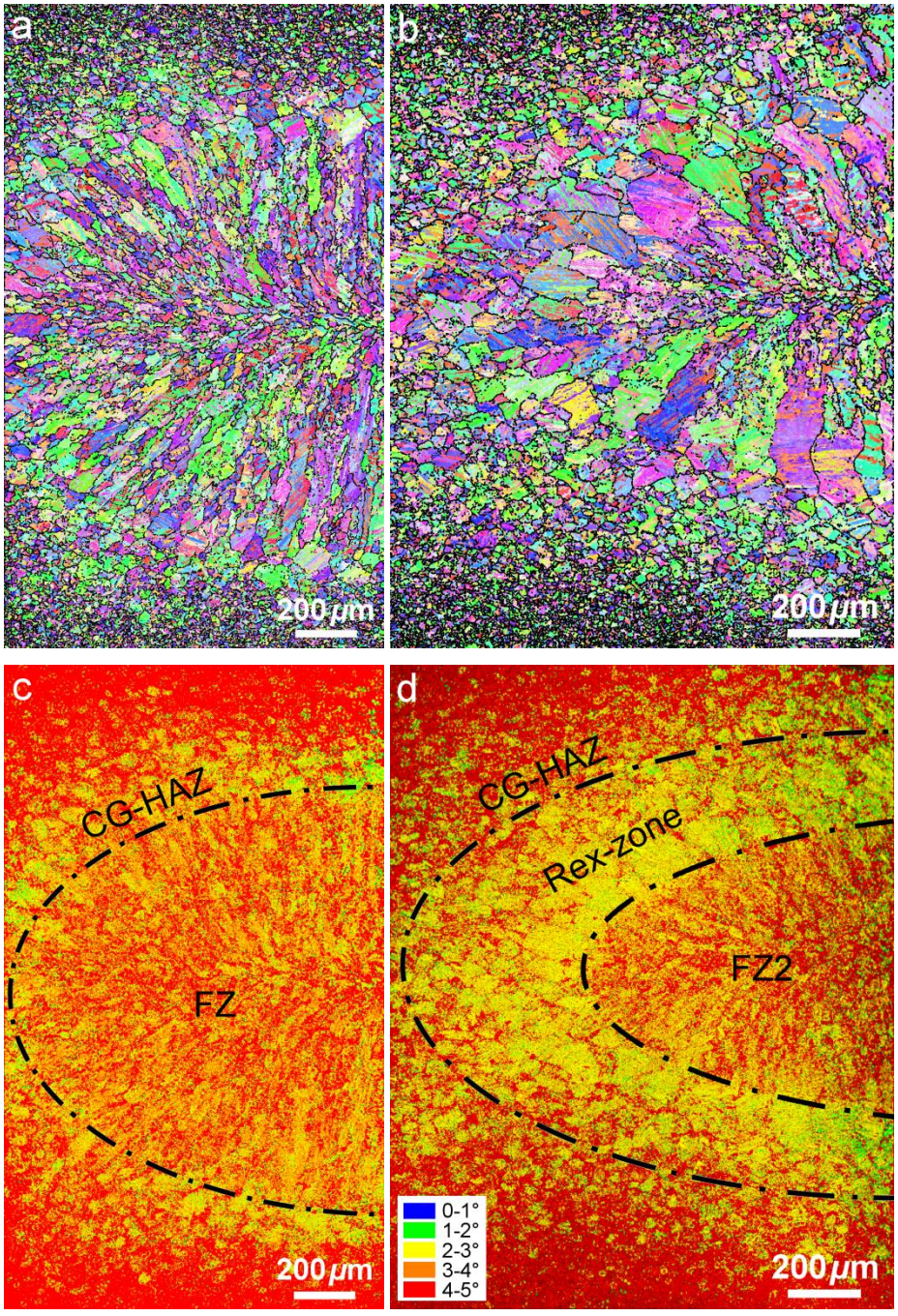

Fig. 9. IPF map and corresponding color coded Kernel average misorientation map of single pulse weld (a, c) and double pulse weld (b, d), respectively.

3.3.2 Crystallographic features of martensite

There exists a similarity between cross-tension test configuration and standard compact tension sample which is used to measure the fracture toughness under mode I loading condition. Here, the interface area surrounding the weld nugget edge acts as the pre-crack that subsequently propagates through the weld nugget under loading. Thus, parameters which affect the fracture toughness of martensite should be studied thoroughly for a better understanding of the mechanical behavior of the welds during the cross-tension test. Toughness affects the speed of a propagating crack [25]. When martensite is tough, the microstructure is resistant against crack propagation and the mean crack velocity is rather low. Accumulation of alloying element such as P along grain boundaries stimulates intergranular fracture in steels because it affects the resistance to shear between the metallic bonds. The relatively low content of P in the investigated DP steel may result in negligible embrittlement. However if it causes segregation at grain boundaries, it would be problematic in the FZ as it is originated from rapid solidification process of RSW. In the case of both single and double pulse welds, fracture occurs outside the FZ, where the segregation of P is insignificant. Considering the low content of P and failure behavior of the welds, it is of importance to study the crystallographic features of martensite which can affect its fracture toughness. The fracture toughness of martensitic microstructure is strongly affected by its resistance to transgranular fracture as the main fracture mode in lath martensite [25]. Transgranular fracture results from rapid propagation of crack along a particular crystallographic plane [26]. For high strength steels with a BCC structure cleavage fracture occurs on {100} planes [25]. The crack path along this plane can be influenced once it approaches a grain boundary. It has been shown that high angle grain boundaries are strong barrier against crack propagation and they are able to arrest or deviate the crack path

effectively [27]. Also, it was reported that high density of high-angle grain boundaries with misorientations larger than 45° enhances the toughness of HAZ of low carbon steel [28].

It is generally accepted that the orientation relationship (OR) between the prior austenite and the resulting martensite in low alloy steels (for example Ni < 28 wt.%) is described by Kurdjumov-Sachs (K-S) relation [29], which is $(111)_\gamma||(011)_{\alpha'}$ and $[\bar{1}01]_\gamma||[\bar{1}\bar{1}1]_{\alpha'}$, namely the close packed planes and directions of marteniste are parallel to those of prior austenite. Theoretically, because of symmetry, a prior austenite grain can transform into 24 different equivalent crystallographic variants. 24 variants of martensite evolved based on K-S OR are denoted as V1-V24 in Table 2. Martensite laths that share the same habit plane of $\{111\}_\gamma$ (e.g. V1 to V6) are aggregated in one packet. Therefore, 24 variants are subdivided into four different packets within one prior austenite grain. Variants can also be divided into three different groups named as Bain groups. A variant of martensite can be evolved from parent austenite by two steps of "Bain strain" and rigid body rotation [30]. Bain strain is associated with contraction in one direction of parent lattice and identical expansion in two other directions. As there are three different selections for compression axes: x, y and z, 24 variants can be grouped into three Bain groups based on compression axes. The misorientation angle and axes of V1 and other 23 variants are also included in Table 2. As illustrated, variants that belong to different Bain groups keep high misorientation angle larger than 47.1°, whereas variants within one Bain group have a low misorientation angle in between (smaller than 21.1°).

Table 2. Misorientation angle/axes between V1 and other variants.

Variant No.	Plane parallel	Direction parallel	Rotation angle / axes from V1	Bain group
V1	$(1\ 1\ 1)_\gamma$//$(0\ 1\ 1)_\alpha$	$[-1\ 0\ 1]_\gamma$//$[-1\text{-}1\ 1]_{\alpha'}$	-	B1
V2		$[-1\ 0\ 1]_\gamma$//$[-1\ 1\text{-}1]_{\alpha'}$	60° / [1 1 -1]	B2
V3		$[\ 0\ 1\text{-}1]_\gamma$//$[-1\text{-}1\ 1]_{\alpha'}$	60° / [0 1 1]	B3
V4		$[\ 0\ 1\text{-}1]_\gamma$//$[-1\ 1\text{-}1]_{\alpha'}$	10.5° / [0 -1 -1]	B1
V5		$[\ 1\text{-}1\ 0]_\gamma$//$[-1\text{-}1\ 1]_{\alpha'}$	60° / [0 -1 -1]	B2
V6		$[\ 1\text{-}1\ 0]_\gamma$//$[-1\ 1\text{-}1]_{\alpha'}$	49.5° / [0 1 1]	B3
V7	$(1\text{-}1\ 1)_\gamma$//$(0\ 1\ 1)_\alpha$	$[\ 1\ 0\text{-}1]_\gamma$//$[-1\text{-}1\ 1]_{\alpha'}$	49.5° / [-1 -1 1]	B2
V8		$[\ 1\ 0\text{-}1]_\gamma$//$[-1\text{-}1\ 1]_{\alpha'}$	10.5° / [1 1 -1]	B1
V9		$[-1\text{-}1\ 0]_\gamma$//$[-1\ 1\ 1]_{\alpha'}$	50.5° / [-10 3 -13]	B3
V10		$[-1\text{-}1\ 0]_\gamma$//$[-1\ 1\text{-}1]_{\alpha'}$	50.5° / [-7 -5 5]	B2
V11		$[\ 0\ 1\ 1]_\gamma$//$[-1\text{-}1\ 1]_{\alpha'}$	14.9° / [13 5 1]	B1
V12		$[\ 0\ 1\ 1]_\gamma$//$[-1\ 1\text{-}1]_{\alpha'}$	57.2° / [-3 5 6]	B3
V13	$(\text{-}1\ 1\ 1)_\gamma$//$(0\ 1\ 1)_\alpha$	$[\ 0\text{-}1\ 1]_\gamma$//$[-1\text{-}1\ 1]_{\alpha'}$	14.9° / [5 -13 1]	B1
V14		$[\ 0\text{-}1\ 1]_\gamma$//$[-1\ 1\text{-}1]_{\alpha'}$	50.5° / [-5 5 -7]	B3
V15		$[-1\ 0\text{-}1]_\gamma$//$[-1\text{-}1\ 1]_{\alpha'}$	57.2° / [-6 -2 5]	B2
V16		$[-1\ 0\text{-}1]_\gamma$//$[-1\ 1\text{-}1]_{\alpha'}$	20.6° / [11 -11 6]	B1
V17		$[\ 1\ 1\ 0]_\gamma$//$[-1\text{-}1\ 1]_{\alpha'}$	51.7° / [-11 6 -11]	B3
V18		$[\ 1\ 1\ 0]_\gamma$//$[-1\ 1\text{-}1]_{\alpha'}$	47.1° / [-24 21 24]	B2
V19	$(1\ 1\text{-}1)_\gamma$//$(0\ 1\ 1)_\alpha$	$[-1\ 1\ 0]_\gamma$//$[-1\text{-}1\ 1]_{\alpha'}$	50.5° / [-3 13 10]	B3
V20		$[-1\ 1\ 0]_\gamma$//$[-1\ 1\text{-}1]_{\alpha'}$	57.2° / [3 6 -5]	B2
V21		$[\ 0\text{-}1\ 1]_\gamma$//$[-1\text{-}1\ 1]_{\alpha'}$	20.6° / [3 0 -1]	B1
V22		$[-1\text{-}1\ 0]_\gamma$//$[-1\ 1\text{-}1]_{\alpha'}$	47.1° / [-10 21 24]	B3
V23		$[\ 1\ 0\ 1]_\gamma$//$[-1\text{-}1\ 1]_{\alpha'}$	57.2° / [-2 -5 -6]	B2
V24		$[\ 1\ 0\ 1]_\gamma$//$[-1\ 1\text{-}1]_{\alpha'}$	21.1° / [9 -4 0]	B1

Fig. 10 shows the IPF maps and misorientation distribution of CG-HAZs and Rex-zone of the two welds. Maps of CG-HAZ were collected from the area exactly close to the boundary of FZ in the single pulse weld and to the Rex-zone of the double pulse weld (see Fig. 8). Statistical analyses reveal that the average prior austenite grain size and martensite packet size of CG-HAZ decreases from 13 and 8.1 μm in single pulse welds to 9.4 and 5.5 μm in double pulse welds, respectively. The average prior austenite grain and packet size in the Rex-zone of double pulse weld close to the pre-crack is 15.6 and 9.2 μm, respectively. Misorientation distribution reveals that the fraction of low angle grain boundaries is higher in the CG-HAZ of the single pulse weld compared to that of the corresponding area of the

double pulse weld. In contrast, the CG-HAZ of the double pulse weld shows the strongest peak at the high-angle grain boundary range (> 47°) and the smallest fraction of low angle grain boundaries (Fig. 10e). Fig. 10f depicts that the Rex-zone of the double pulse weld has the highest fraction of low angle grain boundaries and the lowest fraction of high-angle grain boundaries.

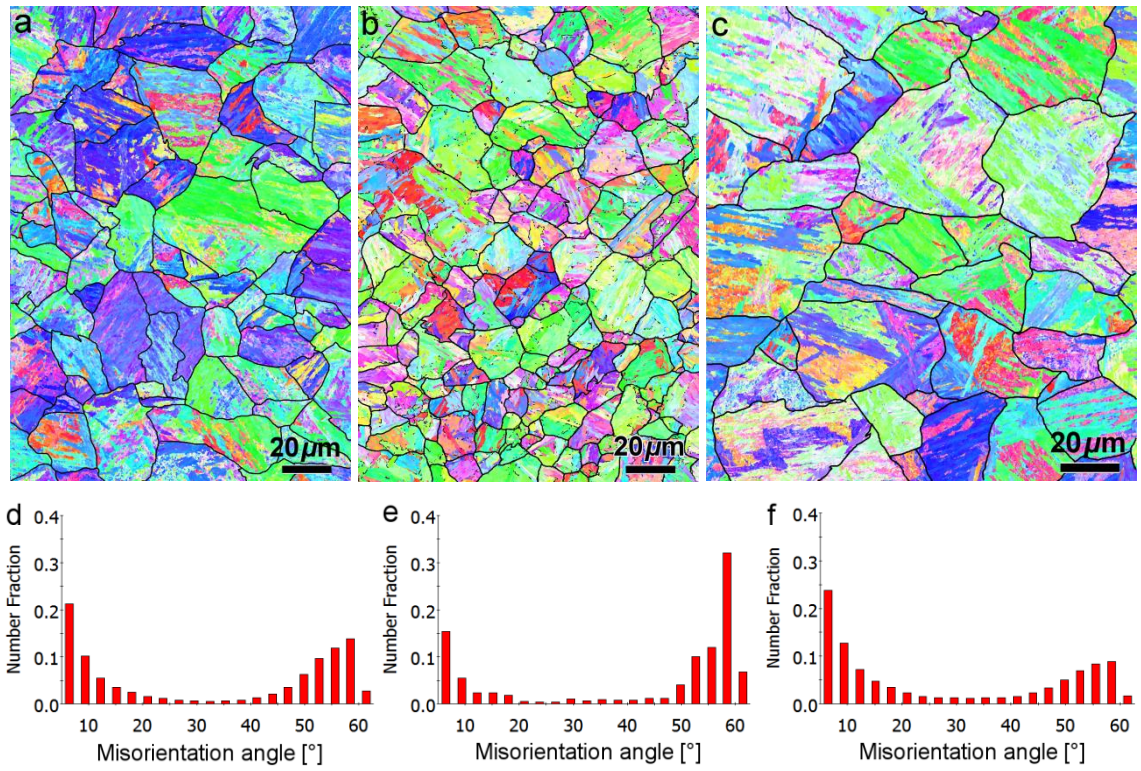

Fig. 10. IPF maps of (a) CG-HAZ of single pulse weld, (b) CG-HAZ and (c) Rex-zone of double pulse weld, with PAGBs shown in black lines. (d-f) Misorientation angle distribution corresponding to (a-c), respectively.

Fig. 11 shows the length fraction of intervariant boundaries between V1 and other variants in the CG-HAZs of the two welds and the Rex-zone of double pulse weld. Variants that belong to the same Bain group are marked with arrows. It is clear that in all three zones most of intervariant boundaries belong to the variants which are within the same crystallographic packets (i.e. V1/ V2-V6). Fig. 11a shows that in the CG-HAZ of single pulse weld the highest fraction of boundaries is V1/V4. These two variants belong to the same Bain group and share

a low misorientation angle of 10.53°. Among inter-packet boundaries, V1/V12(V20) and V1/V8 have higher length fraction. The former one is shared between variants that belong to different Bain group with a high misorientation angle, whereas the latter is shared between variants from the same Bain group with a low misorientation angle. In the CG-HAZ of the double pulse weld the fraction of intervariant boundaries changes significantly (Fig. 11b). In this zone most of boundaries separating blocks of martensite are highly misoriented. Comparison of the intervariant boundary population of the CG-HAZs for the two welds reveals that for the double pulse weld the fraction of V1/V4 noticeably decreases, whereas the fraction of V1/V3(V5) and V1/V2 with high misorientation angle of 60° increases significantly. Fig. 11c shows that the blocks of martensite transformed from the recrystallized austenite are mostly misoriented with low angle boundaries. In this zone the fraction of intervariant boundaries between variants belonging to the same Bain group is higher (i.e., V1, V4, V8). The population of high misorientation angle intervariant boundaries (> 47°) such as V1/V2 and V1/V3(V5) is low, whereas the intra-packet boundary of V1/V4 and inter-packet boundary of V1/V8 depict higher length fraction.

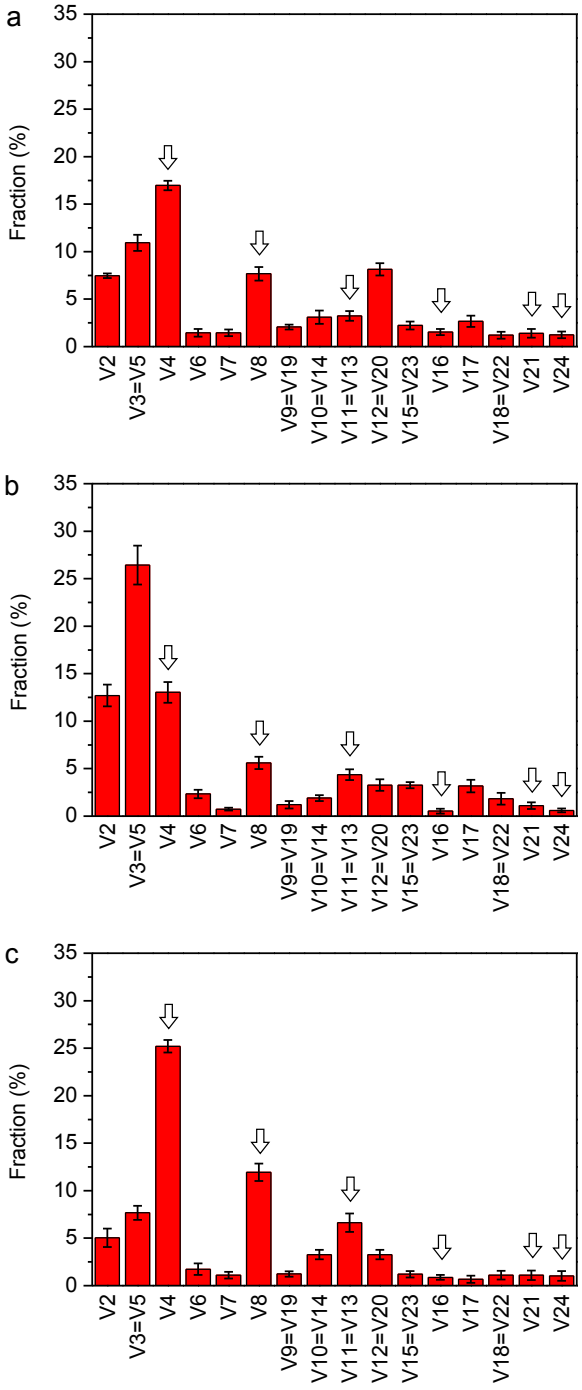

Fig. 11. Length fraction of intervariant boundaries between V1 and other variants in the CG-HAZ of single pulse weld (a), the CG-HAZ (b) and Rex-zone (c) of double pulse weld. Variants of the same Bain group as V1 are marked with arrows.

It is clear that double pulse welding leads to the formation of Rex-zone that shows stronger variant selection as the dominant intervariant boundaries are those belonging to the same Bain group. On the contrary, blocks of martensite in the CG-HAZ of double pulse weld are

misoriented with high-angle boundaries as the most of variants belong to different Bain groups. The variants belonging to different packets and Bain groups are colored in different tints in Fig. 12. The color coding applies to each PAG separately. White and black lines are imposed to the maps indicating the low angle (5-15°) and high angle (> 15°), respectively. Prior austenite grain boundaries are shown with bold black lines. Every single martensite packet is subdivided into two or three Bain groups as indicated in Fig. 12 (d-f). These Bain groups are separated from each other with high-angle boundaries. In addition, each Bain group contains variants of martensite separated with low angle boundaries. Obviously, the density of low angle grain boundaries (white lines) drops significantly in the CG-HAZ of the double pulse weld (see Fig. 12b and 12e). Besides, much finer Bain groups are formed in this zone compared to the CG-HAZ of single pulse and the Rex-zone of the double pulse weld.

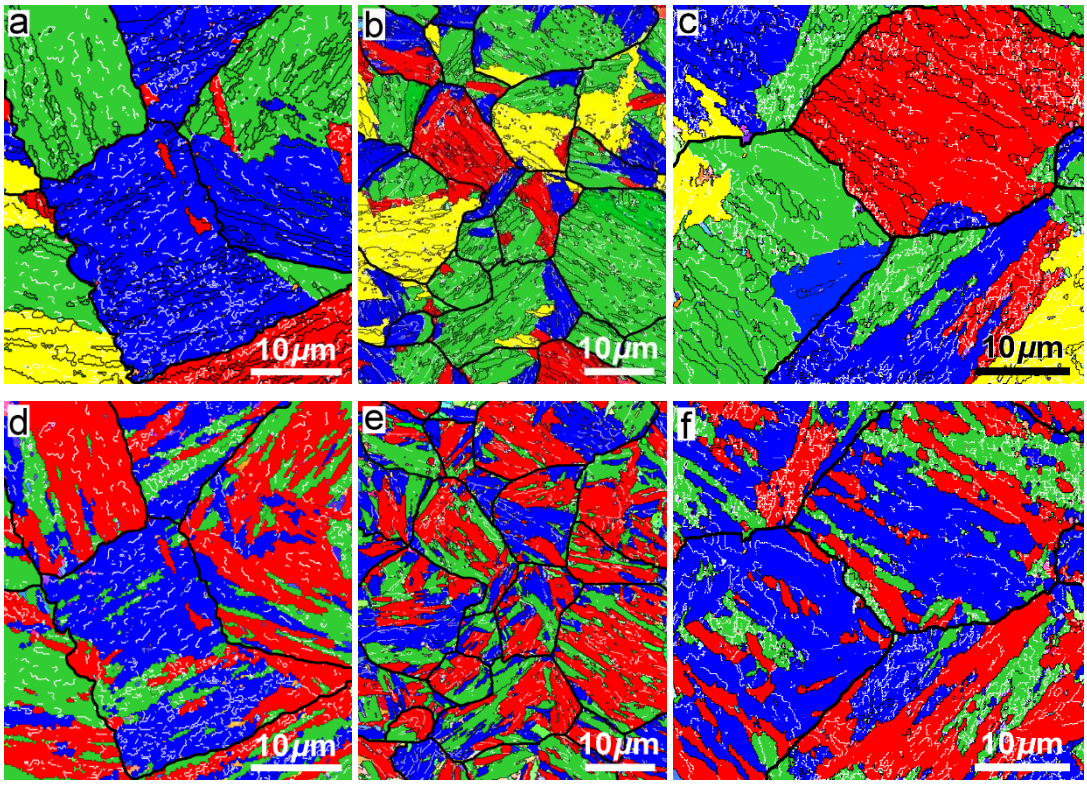

Fig. 12. Packets maps of martensite in CG-HAZ of single pulse weld (a), CG-HAZ (b) and Rex-zone (c) of double pulse weld. (d-f) Bain maps corresponding to (a-c), respectively. White lines indicate low angle (-15°) and black lines are high angle (> 15°) boundaries. PAGBs are shown in bold black lines.

4. Discussion

Improvement in the mechanical performance of resistance spot welded AHSS under peel type loading is considered to be related to two factors: first is the reduction of stress concentration at the weld nugget edge by the SC-HAZ softening. HAZ softening improves the ductility of spot welds and enhance load bearing capacity and energy absorption capability that promote pull-out failure mode [22]. Second is the fracture toughness of the weld nugget, which can be affected by elemental segregation and/or martensite properties. Furusako et al. [23] showed that the fracture toughness at the weld edge strongly affected the strength and failure mode during cross-tension test. They found that post-weld treatment led to an increase in the fracture toughness of the weld and consequently enhanced the strength and load bearing capacity of the weld. Sawanishi et al. [12] investigated the effect of pulsed current via peel tests and showed that the propagation of the crack was arrested much longer for the weld with pulsed current. They attributed the enhancement of the mechanical performance to a higher fracture toughness of the weld resulted from lower segregation of alloying elements such as P and S. However, no significant change in the microstructure of the weld edge was reported. As shown in this study, the weld circumference is severely affected by the second pulse and its microstructure changes significantly. Besides, in the case of both single and double pulse welds, fracture occurs outside the weld nugget but rather through the CG-HAZ where the segregation of P and S is not considerable in comparison with that in the weld nugget.

Summarizing the above observations and analyses demonstrate that large difference in the variant pairing in the different zones of single and double pulse welds is observed. Finer microstructure with larger misorientation angle is achieved in the CG-HAZ of double pulse weld in comparison with its Rex-zone and the CG-HAZ of single pulse welds. The change in the microstructure of martensite in different zones could be explained by the linear elasticity

theory. The variant pairing in shear transformation of lath martensite is a function of both constraint and deformation. In the case of martensitic transformation in unconstrained condition and without deformation, the elastic strain can be relaxed by the formation of single variant of martensite to minimize the surface energy. By contrast, if the growth of martensite lath is limited by its surrounding matrix, the elastic strain is largely relaxed by the formation of new variants with higher misorientation angle belonging to different Bain group [31, 32]. The shear transformation of martensite can be constrained by matrix phase, grain boundaries which interfere with the growth of single variant of martensite and promote formation of variants with larger misorientation angle with respect to each other. The peak temperature experienced by the Rex-zone of double pulse weld is obviously higher than its CG-HAZ leading to recrystallization of the austenite at high temperatures. Recrystallization is associated with the migration of high-angle grain boundaries and rearrangements of dislocation configurations. Higher peak temperature exposed at the Rex-zone homogenizes the matrix and decreases the density of defects. Growth of austenite grains may also occur, leading to more homogenization of matrix and reduction of fraction of prior austenite grain boundaries. Thus, the factors that constrain the martensitic transformation at the Rex-zone are less effective. This culminates in martensitic microstructure with a stronger variant selection in which coarser Bain groups with high fraction of low angle grain boundaries are formed. The finer microstructure of CG-HAZ in the double pulse weld could be attributed to the reverse transformation of austenite at lower temperatures. Lower peak temperature at CG-HAZ compared to the Rex-zone avoids recrystallization and growth of prior austenite grains. Also rapid cooling after the first pulse may lead to partial transformation of austenite to ferrite or even bainite or martensite. The second phase can split and break the initial austenite grains. Once the second pulse is applied reverse austenite transformation occurs at the CG-HAZ. During the second pulse, the second phase and austenite boundaries may act as

favorable nucleation sites for the formation of new austenite grains resulting in finer prior austenite grains. Furthermore, dislocations induced by the electrode force after the first pulse, although less favorable sites compared to grain-boundaries, may also act as heterogeneous nucleation sites. As the peak temperature is lower than recrystallization temperature, these dislocations may remain in the microstructure leading to the formation of finer prior austenite grains. The prior austenite grains are strong constraint against the growth of lath martensite. As a result smaller martensite packets and Bain groups are formed inside the prior austenite grain (see Fig. 12). This is similar to the refinement of prior austenite grains by thermal cycling in which reverse transformation of martensite to austenite is applied to refine the size of austenite grains [33-36]. However, it should be noted that further investigations are essential to study thermal history and phase transformation kinetics during single and double pulsed RSW.

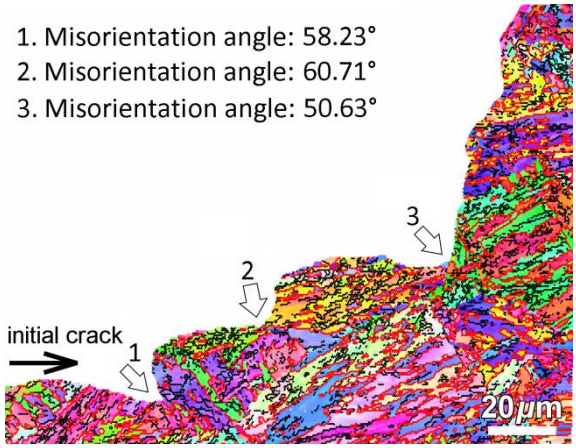

Fig. 13. IPF map of a fractured double pulse weld (black lines indicate boundaries with misorientation between 15 and 50°, red lines show the boundaries with misorientation higher than 50°).

Fig. 13 shows the IPF map of the crack propagation path inside the Rex-zone of a double pulse weld. Pre-crack and its direction are shown by a black arrow. Grain boundaries with misorientation between 15° and 50° are shown in black lines and grain boundaries with

misorientation larger than 50° are imposed by red lines. Three main deflection points of cracking path combined with misorientation angle of grain boundaries are highlighted. As illustrated, the crack is strongly deflected once it crosses over grain boundaries with misorientation higher than 50°. It confirms that the fracture toughness of the weld and crack propagation are strongly dependent on the morphological and crystallographic characteristics of martensite phase formed during RSW.

Although the weld nugget size is the same for both single and double pulse welds, larger fracture area is obtained for the double pulse weld as the failure occurs in the SC-HAZ on one side of the weld. The microstructural characteristics and fracture behavior of the resistance spot welded DP1000 steel samples can be summarized in Fig. 14. Crack in the single pulse weld immediately deflected toward the CG-HAZ. In the case of double pulse weld, on one side of the weld, crack penetrates small distance into the Rex-zone. Rex-zone has coarse structure of Bain groups and low fraction of high-angle grain boundaries. However, this area is thick enough and contains reasonable number of equiaxed prior austenite grains containing packets and Bain groups. Prior austenite grains, martensite packet and Bain group boundaries are considered having high-angle boundaries that are effective in arresting the crack propagation as more energy is needed for crack to propagate through. Thus, the crack path deviates towards CG-HAZ since it is forced to cross over several equiaxed prior austenite grains in the Rex-zone. Prior austenite grains are finer at the CG-HAZ of double pulse weld and lead to smaller packets of martensite. Besides, variant pairing in this zone results in the evolution of martensitic microstructure with finer Bain groups. Boundaries along these Bain groups are highly misoriented and can effectively arrest and deflect cracks. On the other side, the failure occurs at the SC-HAZ and results from severe softening of martensite. The better mechanical performance of double pulse weld can be explained by three factors. First, double pulse welding generates softer SC-HAZ which acts

as failure location at one side of the weld. Second, on the other side, crack starts and propagates firstly in the Rex-zone which has a lower residual strain compared to its surrounding zones. Thus, the crack propagation is slow although it has a lower fraction of high-angle boundaries and coarser Bain groups. And third, after penetration into the Rex-zone, crack path deviates through the CG-HAZ that has a high fraction of high-angle boundaries and finer structure of prior austenite grains, martensite packets and Bain groups that retard crack propagation. It should be noted that the cross-tension loading of resistance spot welds is complex since it involves a non-homogeneous geometry, with a non-homogeneous microstructure subjected to a non-homogeneous loading conditions. To identify the specific contributions of all parts of the weld zone would require even more localized testing of specific parts of the weld microstructure.

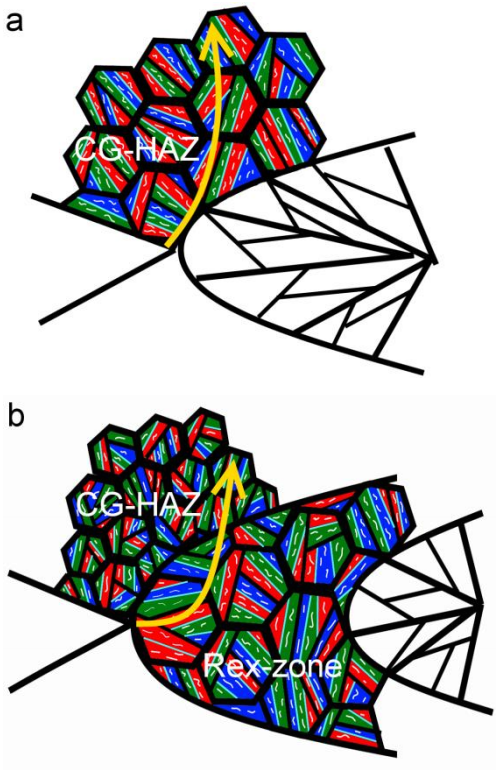

Fig. 14. Schematic sketch showing the microstructure and crack path in single pulse weld (a) and double pulse weld (b). Prior austenite grain boundaries and martensite packet boundaries are shown in bold black lines, Bain group boundaries and low angle grain boundaries are shown in cyan and white lines, respectively.

5. Conclusions

The effects of welding parameters on the cross-tension strength, failure behavior and microstructural evolution of DP1000 steel were investigated. Two RSW processes with single and double pulse current were applied.

The main conclusions are summarized as follow:

1) Double pulse welding enhances cross-tension strength and energy abortion capability of the weld compared to the sample welded with single pulse process. Maximum load for the weld size of 7 mm and sheet thickness of 1.5 mm increases from 9.2 kN for single pulse weld to 11.7 kN for double pulse weld. The absorbed energy of the single pulse weld at maximum load is 55.3 J. This value rises to 75.2 J with applying the second pulse. Larger plug diameter with the average of 7.4 mm is achieved for the double pulse weld compared to the plug diameter of single pulse with the average of 7 mm.
2) Double pulse welding leads to the formation of softer SC-HAZ. Besides, it creates Rex-zone with lower hardness and lower residual strain. Residual strain was qualitatively studied using KAM values.
3) It is found that the weld scheme strongly affects the crystallographic features of martensite phase that forms at different weld zones.
4) Grain boundary characterization shows that a low fraction of high-angle grain boundaries and coarser structure of Bain groups are formed in the Rex-zone of double pulse welds.
5) Finer structure of prior austenite grains, martensite packets and Bain groups are formed in the CG-HAZ of double pulse weld.

6) Better mechanical performance of double pulse welds of DP1000 dual phase steel is attributed to three main factors: first, severe softening at the SC-HAZ of double pulse weld leading to reduction in the stress concentration around the weld edge during mode I loading which stimulates failure outside the weld; second, formation of thick Rex-zone with lower residual strain; third, CG-HAZ containing a large fraction of high angle grain boundaries acting as obstacles for crack propagation and a fine structure of Bain groups.

Acknowledgement

This research was carried out under project number T22.7.13508 in the framework of the Partnership Program of the Materials innovation institute M2i (www.m2i.nl) and the Netherlands Organization for Scientific Research (www.nwo.nl).

References

[1] N. Baluch, Z. M. Udin, C. S. Abdullah, Advanced high strength steel in auto industry: an Overview, Eng. Tech. Appl. Sci. Res. 4 (2014) 686-689.

[2] F. Nikoosohbat, S. Kheirandish, M. Goodarzi, M. Pouranvari, S. P. H. Marashi, Microstructure and failure behaviour of resistance spot welded DP980 dual phase steel, Mater. Sci. Technol. 26 (2010) 738-744.

[3] S. Dancette, V. Massardier-Jourdan, D. F. J. Merlin, T. Dupuy, M. Bouzekri, HAZ microstructures and local mechanical properties of high strength steels resistance spot welds, ISIJ Int. 51 (2011) 99-107.

[4] S. Sam, M. Shome, Static and fatigue performance of weld bonded dual phase steel sheets, Sci. Tech. Weld. Join. 15 (2010) 242-247.

[5] M. Pouranvari, S. P. H. Marashi, Key factors influencing mechanical performance of dual phase steel resistance spot welds, Sci. Tech. Weld. Join. 15 (2010) 149-155.

[6] M. Pouranvari, S. P. H. Marashi, S. M. Mousavizadeh, Failure mode transition and mechanical properties of similar and dissimilar resistance spot welds of DP600 and low carbon steels, Sci. Tech. Weld. Join. 15 (2010) 625-631.

[7] V. H. Baltazar Hernandez, S. K. Panda, Y. Okita, N. Y. Zhou, A study on heat affected zone softening in resistance spot welded dual phase steel by nanoindentation, J. Mater. Sci. 45 (2010) 1638-1647.

[8] W. Tong, H. Tao, N. Zhang, et al., Deformation and fracture of miniature tensile bars with resistance-spot-weld microstructures, Metall. Mater. Trans. 36 (2005) 2651-2669.

[9] M. D. Tumuluru, Resistance spot welding of coated high-strength dual-phase steels, Weld. J. 85 (2006) 31-37.

[10] M. Pouranvari, S. P. H. Marashi, S. M. Mousavizadeh, Dissimilar resistance spot welding of DP600 dual phase and AISI 1008 low carbon steels: correlation between weld microstructure and mechanical properties, Ironmaking & Steelmaking 38 (2011) 471-480.

[11] S. Dancette, D. Fabrègue, V. Massardier, J. Merlin, T. Dupuy, M. Bouzekri, Experimental and modeling investigation of the failure resistance of Advanced High Strength Steels spot welds, Eng. Fract. Mech. 78 (2011) 2259-2272.

[12] C. Sawanishi, T. Ogura, K. Taniguchi, et al., Mechanical properties and microstructures of resistance spot welded DP980 steel joints using pulsed current pattern, Sci. Tech. Weld. Join. 19 (2014) 52-59.

[13] M. Mimer, L. E. Svensson, R. Johansson, Process adjustments to improve fracture behaviour in resistance spot welds of EHSS and UHSS, Weld. World 48 (2004) 14-18.

[14] X. Liao, X. Wang, Z. Guo, M. Wang, Y. Wu, Y. Rong, Microstructures in a resistance spot welded high strength dual phase steel, Mater. Character. 61 (2010) 341-346.

[15] E. M. v. d. Aa, M. Amirthalinham, J. Winter, I. M. Richardson, Improved resistance spot weldability of 3rd generation AHSS for automotive applications, presented at the International Seminar on Numerical Analysis of Weldability, Graz, Seggau, Austria, 2015.

[16] STAHL-EISEN-Prüfblätter des Stahlinstituts VDEh, SEP 1220-2: Testing and documentation guideline for the joinability of steel sheet Part 2: resistance spot welding, 2008.

[17] M. Pouranvari, S. P. H. Marashi, Critical review of automotive steels spot welding: process, structure and properties, Sci. Tech. Weld. Join. 18 (2013) 361-403.

[18] D. J. Racovic, M. Tumuluru, An evaluation of the cross-tension test of resistance spot welds in high-strength dual-phase steels, Weld. J., 91 (2012) (8-15).

[19] V. H. B. Hernandez, M. L. Kuntz, M. I. Khan, Y. Zhou, Influence of microstructure and weld size on the mechanical behaviour of dissimilar AHSS resistance spot welds, Sci. Tech. Weld. Join. 13 (2008) 769-776.

[20] M. Xia, E. B. Z. Tian, Y. N. Zhou, Effects of heat input and martensite on HAZ softening in laser welding of dual phase steels, ISIJ Int. 48 (2008) 809-814.

[21] V. H. Baltazar Hernandez, S. S. Nayak, Y. Zhou, Tempering of martensite in dual-phase steels and its effects on softening behavior, Metallur. Mater. Trans. A, 42 (2011) 3115-3129.

[22] M. Pouranvari, Effect of resistance spot welding parameters on the HAZ softening of DP980 ferrite-martensite dual phase steel welds, World Appl. Sci. J. 10 (2011) 1454-1458.

[23] S. Furusako, F. Watanabe, G. Murayama, et al., Current problems and the answer techniques in welding technique of auto bodies, Nippon Steel Technical Report 1995 (2013) 25-31.

[24] C. Cayron, ARPGE: a computer program to automatically reconstruct the parent grains from electron backscatter diffraction data, J. Appl. Cryst. 40 (2007) 1183-1188.

[25] J.J. Jonas, Effect of austenite recrystallization on toughness of pipeline steels, Mater. Sci. Forum 753 (2013) 546-553.

[26] T. L. Anderson, Fracture Mechanics: Fundamentals and Applications, CRC Press, 2005.

[27] A. Lambert-Perlade, T. Sturel, A. F. Gourgues, J. Besson, A. Pineau, Mechanisms and modeling of cleavage fracture in simulated heat-affected zone microstructures of a high-strength low alloy steel, Metall. Mater. Trans. A 35 (2004) 1039-1053.

[28] Y. You, C. Shang, N. Wenjin, S. Subramanian, Investigation on the microstructure and toughness of coarse grained heat affected zone in X-100 multi-phase pipeline steel with high Nb content, Mater. Sci. Eng. A 558 (2012) 692-701.

[29] H. K. D. H. Bhadeshia, R. W. K. Honeycombe, Steels microstructure and properties, Third edition, Butterworth-Heinemann, 2006.

[30] H. K. D. H. Bhadeshia, Worked examples in the Geometry of Crystals: The Institute of Metals, 1987.

[31] P. Xu, J. W. Morris, Computer simulation of microstructure, Metall. Trans. A 23 (1992) 2999-3012.

[32] P. Xu, J. W. Morris, Computer simulation of martensitic transformations in constrained, two-dimensional crystals under external stress, Metall. Trans. A 24 (1993) 1281-1294.

[33] J. Hidalgo, M. J. Santofimia, Effect of prior austenite grain size refinement by thermal cycling on the microstructural features of as-quenched lath martensite, Metall. Mater. Trans. A 47 (2016) 5288-5301.

[34] T. Furuhara, K. Kikumoto, H. Saito, et al., Phase transformation from fine-grained austenite, ISIJ Int. 48 (2008) 1038-1045.

[35] J. t. Zhang, Y. g. Zhao, J. Tan, X. f. Xu, Austenite grain refinement by reverse $\alpha' \rightarrow \gamma$ transformation in metastable austenitic manganese steel, J. Iron Steel Res. Int. 22 (2015) 157-162.

[36] J. Liu, G. Wen, Y. Li, P. Tang, L. Luo, Effect of $\gamma \rightarrow \alpha$ phase transformation on refining austenite grains of microalloyed steel in continuous casting by simulation, High Temp. Mater. Proc. 35 (2016) 653-659.